JGR Solid Earth

RESEARCH ARTICLE
10.1029/2025JB032025

Key Points:

- The first three-dimensional crustal-scale shear velocity model of Mutnovsky and Gorely area was constructed using ambient noise tomography
- A low-velocity zone at 2–5 km beneath Mutnovsky marks a magma chamber; a similar zone under Gorely at 2–4 km indicates intrusion
- Low-velocity zones at 2–5 and 0.5–1 km beneath the Mutnovsky Geothermal Power Plant mark intrusion and production intervals, respectively

Supporting Information:

Supporting Information may be found in the online version of this article.

Correspondence to:

N. Belovezhets,
n.belovezhets@gmail.com

Citation:

Belovezhets, N., Berezhnev, Y., Abramenkov, S., Abkadyrov, I., Dergach, P., Khmarin, E., et al. (2026). Crustal sources of geothermal and magmatic activity in the area of Mutnovsky-Gorely volcanic complex (Kamchatka) inferred from ambient noise tomography. *Journal of Geophysical Research: Solid Earth*, *131*, e2025JB032025. https://doi.org/10.1029/2025JB032025

Received 17 MAY 2025
Accepted 18 DEC 2025

Author Contributions:

Conceptualization: N. Belovezhets, Y. Berezhnev, I. Koulakov
Data curation: N. Belovezhets, Y. Berezhnev, S. Abramenkov, I. Abkadyrov, P. Dergach, D. Chebrov, I. Koulakov
Formal analysis: N. Belovezhets, Y. Berezhnev, I. Koulakov
Funding acquisition: E. Khmarin, I. Koulakov
Investigation: N. Belovezhets, Y. Berezhnev, I. Koulakov
Methodology: N. Belovezhets, Y. Berezhnev, I. Koulakov
Project administration: S. Abramenkov, I. Abkadyrov, P. Dergach, E. Khmarin, I. Koulakov

Crustal Sources of Geothermal and Magmatic Activity in the Area of Mutnovsky-Gorely Volcanic Complex (Kamchatka) Inferred From Ambient Noise Tomography

N. Belovezhets[1], Y. Berezhnev[1], S. Abramenkov[2,3], I. Abkadyrov[4], P. Dergach[3], E. Khmarin[5], D. Chebrov[6], and I. Koulakov[1,3]

[1]Skolkovo Institute of Science and Technology, Moscow, Russia, [2]Novosibirsk State University, Novosibirsk, Russia, [3]Trofimuk Institute of Petroleum Geology and Geophysics of the Siberian Branch of the Russian Academy of Sciences, Novosibirsk, Russia, [4]Institute of Volcanology and Seismology of the Far Eastern Branch of the Russian Academy of Sciences, Petropavlovsk-Kamchatsky, Russia, [5]LLC "ZN Geotherm" (JSC "Zarubezhneft"), Moscow, Russia, [6]Kamchatka Branch of the Geophysical Service of the Russian Academy of Sciences, Petropavlovsk-Kamchatsky, Russia

Abstract The Mutnovsky and Gorely volcanoes in Kamchatka, located 70–80 km southwest of Petropavlovsk-Kamchatsky, pose significant hazard due to their potential for explosive eruptions. Mutnovsky also hosts the Mutnovsky Geothermal Power Plant (MGPP). This study presents the first crustal-scale three-dimensional seismic velocity model derived from ambient noise tomography, utilizing data from a temporary 2023–2024 seismic network of 65 mixed broadband and short-period stations, in addition to four permanent stations. The model reveals multiple low-velocity zones: a low-velocity anomaly at 2–5 km depth below sea level is interpreted as a Mutnovsky magma chamber, while the other one at 2.5–5 km depth beneath the MGPP likely reflects an active magmatic intrusion sustaining the geothermal system. A shallow anomaly at 0.5–1 km depth beneath the MGPP is attributed to production intervals associated with geothermal boreholes. Furthermore, the model indicates hydrothermal connectivity between the Mutnovsky field and the Zhirovskoy Valley, with no apparent connection to the Vilyuchinsky Valley springs. Beneath the Gorely caldera, a wide low-velocity zone suggests the presence of unconsolidated sediments and an underlying magmatic intrusion at 2–4 km depth.

Plain Language Summary Mutnovsky and Gorely are active volcanoes in Kamchatka with the substantial potential of explosive eruptions. Mutnovsky volcano also hosts a sizable geothermal power plant. To better understand the magmatic and hydrothermal systems beneath these volcanoes, we installed a network of seismic stations and used the data to create the first 3-D velocity model of the subsurface. We found the slow velocity zones beneath Mutnovsky and Gorely at depths of 2–5 km below sea level, and beneath the power plant at depths of 2–5 km and 0.5–1 km. The slower velocity likely indicates the presence of fluids such as magma or water within rock pores. Based on their depth and geological context, the zone beneath Mutnovsky outlines the magma chamber, while those beneath Gorely and the power plant at 2–5 km indicate hot magmatic intrusions. The shallow slow velocity zone beneath the power plant likely illustrates water-saturated rocks used for geothermal energy production. We also found the connectivity between hydrothermal springs near Mutnovsky volcano and in the Zhirovskoy Valley, but no apparent connection to the Vilyuchinsky Valley springs.

1. Introduction

This study investigates the crustal structures surrounding the active Mutnovsky and Gorely volcanoes in the central-eastern Kamchatka Peninsula. Located approximately 70–80 km from Petropavlovsk-Kamchatsky, with a population of ~200,000, these volcanoes are easily accessible and serve as major tourist attractions. However, both volcanoes pose significant risks to the region's population and infrastructure (Girina et al., 2018). Geophysical monitoring and multiscale investigations of the deep structures beneath these volcanoes are essential for identifying potential eruption scenarios.

The study area includes the Mutnovsky and Verkhne-Mutnovsky Geothermal Power Plants (MGPP), a coupled system constructed between 1999 and 2001. Together, they produce 62 MW of electrical energy, supplying approximately 20%–30% of Central Kamchatka's energy demand. Moreover, the region has significant potential to expand capacity up to 1 GW (Kiryukhin & Sugrobov, 2019), which could decrease dependence on

Resources: I. Abkadyrov, P. Dergach, D. Chebrov, I. Koulakov
Software: N. Belovezhets, Y. Berezhnev, I. Koulakov
Supervision: I. Koulakov
Validation: N. Belovezhets, Y. Berezhnev, S. Abramenkov, I. Koulakov
Visualization: N. Belovezhets, Y. Berezhnev, S. Abramenkov, I. Koulakov
Writing – original draft: N. Belovezhets, Y. Berezhnev, I. Koulakov
Writing – review & editing: N. Belovezhets, Y. Berezhnev, S. Abramenkov, D. Chebrov, I. Koulakov

environmentally damaging and costly fossil fuels. Geophysical surveys of the crust near the MGPP are necessary for assessing the distribution of potential geothermal resources.

For several decades, the Kamchatkan Branch of the Geophysical Survey (KB GS) of the Russian Academy of Sciences has continuously monitored the Gorely and Mutnovsky volcanoes through video surveillance and seismological records analysis, providing daily activity reports (Chebrov et al., 2013; Senyukov, 2013). KB GS maintains one seismic station on Gorely (GRL), one on Mutnovsky (MTV), and two additional remote stations in the surrounding region (ASA and RUS) (Figure 1). The Institute of Volcanology and Seismology of the Far Eastern Branch of the Russian Academy of Sciences (IVS FEB RAS) also contributes to monitoring efforts through satellite remote sensing and periodic field observations (KVERT). Despite limited station coverage, ongoing monitoring has successfully localized relatively strong seismic events and documented the seismicity background (e.g., Kugaenko & Nuzhdina, 2009).

Several multiscale seismic tomography models have been obtained in the study area using data from both permanent and temporary networks. Regional and global tomography studies (Bijwaard et al., 1998; Gorbatov et al., 2001; Jiang et al., 2009; Koulakov et al., 2011) have clearly identified a high-velocity slab in the upper mantle beneath Kamchatka, as well as distribution of seismicity in the Benioff zone (Lander & Shapiro, 2007). However, the density of permanent station coverage has been insufficient for investigating shallower structures corresponding to the mantle wedge and crust, locating microseismic events or revealing the structural features beneath the volcanoes, as demonstrated by previous tomographic studies (Gontovaya et al., 2008; Koulakov, Kukarina, et al., 2016). Significant progress in studying the crustal and uppermost mantle structures beneath Central Kamchatka was made with the deployment of a regional temporary seismic network in 2019–2020, consisting of 30 seismic stations alongside the existing permanent stations. Bushenkova et al. (2023) used data from this network to construct a seismic tomography model based on body waves from local seismicity, while Egorushkin et al. (2024) created another model using surface waves from ambient noise cross-correlations. Although these models cover part of the study area, including Mutnovsky and Gorely volcanoes, their resolution is still limited for robust identification of the magmatic and hydrothermal systems detailed structure in the crust.

Several local-scale studies have provided structural details beneath specific parts of the study area. For example, between 2013 and 2014, a temporal seismic network of 20 stations was deployed on Gorely Volcano. Kuznetsov et al. (2017) used data from this network for local earthquake tomography, revealing zones beneath the volcanic edifice that were saturated with gases and liquid fluids. These zones were likely responsible for the volcano's intense degassing activity observed during the study period (Aiuppa et al., 2012). Additionally, the same data was used to investigate long-period seismic events associated with the degassing process (Abramenkov et al., 2020).

Interdisciplinary local-scale geophysical studies have been conducted in the Mutnovsky geothermal field to support the exploration and exploitation of its geothermal resources. Several studies have described combined electromagnetic, gravity, and magnetometric surveys (Belousov et al., 2005; Pahkevich et al., 2018; Spichak et al., 2007). A three-dimensional geoelectric model of the Mutnovsky geothermal field was constructed using magnetotelluric data (Nurmukhamedov et al., 2010). Additionally, a local temporal network of 10 stations, installed on the Verkhne-Mutnovsky geothermal field with an aperture of approximately 1 km, identified seismic emission zones linked to geothermal activity at depths of 1–2 km (Kugaenko et al., 2004).

A temporal seismic network deployed in 2023–2024 across Mutnovsky, Gorely, and the surrounding areas was designed to cover a middle-scale gap between regional and local-scale seismic surveys. In this study, we for the first time analyze continuous seismic data from this network using ambient noise tomography to create a three-dimensional model of shear wave velocity in the upper crust down to approximately 10 km. This model is crucial for identifying the crustal roots of magma plumbing systems beneath Mutnovsky and Gorely volcanoes, which can aid in assessing potential eruption scenarios. Additionally, it provides insights into the localization of heating zones beneath the hydrothermal systems of these volcanoes, which is valuable for identifying prospective areas for geothermal energy exploitation and expanding the capacity of the Mutnovsky Geothermal Plant.

2. Geological Settings

The study region's geological development is primarily driven by the ongoing subduction of the mature Pacific Plate with the age of 90–105 Ma along the Kuril-Kamchatka arc (e.g., Syracuse & Abers, 2006). Kamchatka exhibits all the characteristics of a classical subduction zone, including a clearly traced Benioff zone of deep

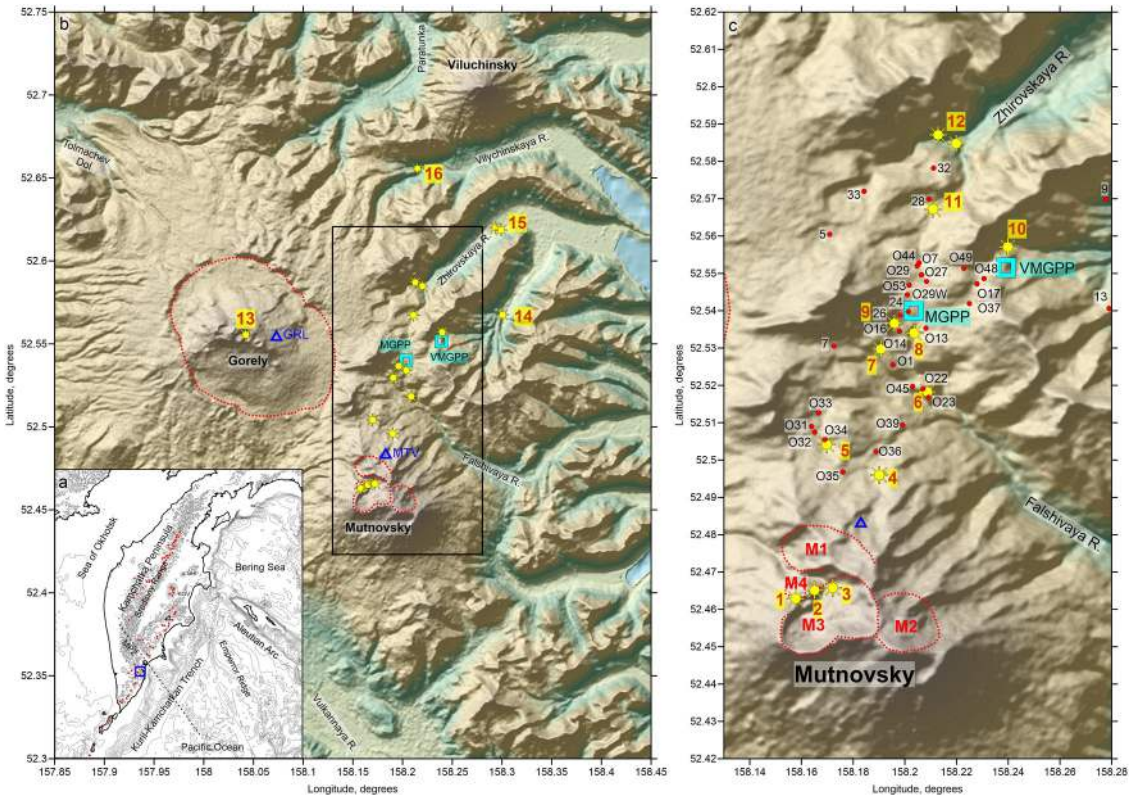

Figure 1. Study area. (a) Map of the Kamchatka Peninsula with the location of the study area indicated with the blue rectangle. The red dots depict the Holocene volcanoes, and contour lines indicate the relief. (b) Topography map of the study area. The red dotted lines highlight the caldera of Gorely Volcano and the volcanic centers of Mutnovsky Volcano edifice. The blue triangles depict the permanent seismic stations of KB GS RAS. Blue squares indicated by MGPP and VMGPP are the Mutnovsky and Verkhne-Mutnovsky Power Plants. The yellow symbols are locations of hydrothermal discharges (fumaroles and hot springs): (1) Mutnovsky Active Crater; (2, 3) Donnoe and Upper fumarolic fields; (4, 5) North-Mutnovsky Fields; (6) New 2003; (7) Dachny; (8) Radon; (9) Medvezhy; (10) V-Mutnovsky; (11) Piratovsky hot springs; (12) V-Zhirovskoy; (13) Gorely Crater Fumarole; (14) Voinovsky Springs; (15) N-Zhirovskoy fumaroles and hot springs; (16) Viluchinsky hot springs. (c) Enlarged area (corresponding to the black rectangle in panel (b)) of the Mutnovsky hydrothermal field with boreholes indicated by the red dots. M1, M2, M3 and M4 indicate four volcanic centers of Mutnovsky.

seismicity (Lander & Shapiro, 2007), a well-developed trench, a continuous volcanic arc, and manifestations of back-arc volcanism. Nevertheless, the complex interactions between the oceanic plate, which contains island arcs and seamount remnants, and the overlying continental lithosphere have led to distinct tectonic features that cannot be modeled by a simple two-dimensional conveyor-type subduction model. In particular, to the north of the study area, the Malko-Petropavlovsk zone of lateral dislocations marks a transition in the subduction regime between the central and southern segments of Kamchatka around the latitude of ∼53° (Avdeiko et al., 2006; Gordeev & Bergal-Kuvikas, 2022). To the south, where the study area is located, the slab is older (100–105 Ma) compared to the northern segment and dips with an angle of approximately 45° (Gorbatov et al., 1997; Syracuse & Abers, 2006) down to at least 600 km, as marked by seismicity in the Benioff zone (Lander & Shapiro, 2007; Levina et al., 2013).

The South Kamchatkan volcanic front presents a continuous arc of long-living volcanic complexes that started developing in the Late Oligocene (Avdeiko et al., 2006). Our study area includes active volcanoes (Gorely, Mutnovsky) and the extinct Vilyuchinsky and Asacha volcanoes, each with distinct eruptive histories, structural features, and geophysical characteristics. Mutnovsky and Gorely volcanoes align along a trench-perpendicular lineament following toward the Tolmachev Dol, where recent monogenic volcanic activity was observed (Ponomareva et al., 2007; Figure 1). The gradual increase in the subducting slab's depth along this line from ∼90 to 100 km below Mutnovsky to ∼120 km below Gorely determines different eruption regimes and compositions of these volcanic complexes (Duggen et al., 2007; Gorbatov, 1999).

Below, we provide a brief overview of these volcanoes, focusing on their geological evolution, recent activity, and studies that have illuminated their subsurface structures and magmatic systems.

Gorely Volcano has a complex evolutionary history and currently presents as a flat stratovolcano with a relative elevation of ~800 m and an absolute altitude of 1,799 m. The volcano is situated within an elliptical caldera, measuring 9 × 13 km (outlined by the red dotted line in Figure 1), which was formed by a powerful explosive eruption that ejected approximately 100 km^3 of andesitic to andesitic-dacitic tephra (Braitseva et al., 1995) or by multiple eruptions forming several nested calderas (Bindeman et al., 2010; Seligman et al., 2014). While most studies date this eruption to 38–40 ka (Selyangin, 2009), additional dating suggests that some of Gorely's welded tuffs may originate from older mid-Pleistocene eruptions, around 361 ka (Bindeman et al., 2010).

Post-caldera activity at Gorely has produced extensive Hawaiian-type lava flows, primarily composed of basalt and andesitic-basalt, which originated from the summit crater and several flank cinder cones (Seligman et al., 2014). During the Holocene, the volcano has exhibited moderate explosive and effusive activity. The most recent magmatic eruption in 1986 created a large crater now occupied by a lake, with several active fumaroles. Between 2010 and 2013, Gorely experienced intense degassing, with gas fluxes reaching up to 11,000 tons per day (Aiuppa et al., 2012).

At the margin of the study area lie two large stratovolcanoes, *Viluchinsky* and *Asacha*, both currently considered dormant. *Viluchinsky Volcano*, with an elevation of 2,175 m, primarily formed during the Late Pleistocene. In the Early Holocene, approximately 7,600–10,000 years ago, the volcano produced a lava flow and moderate fallout from basaltic-andesite cinder cones (Romanova et al., 2015). Hydrothermal activity is evident on the southeastern flanks of Vilyuchinsky, and minor gas emissions from the summit were reported in the 1950s (Sirin, 1958). *Asacha Volcano*, with an elevation of 1,910 m, is located to the southwestern side of the Mutnovsky and Gorely. It initially formed as a shield basaltic volcano, which was later overlain by several Pleistocene lava cones. During the Holocene, several basaltic cinder cones and lava flows developed on its western and southern flanks (Kozhemyaka et al., 1988). In 1983, a significant seismic unrest was observed (Tokarev, 1984), but it did not result in volcanic activity. These observations suggest that both Vilyuchinsky and Asacha may still exhibit some level of volcanic activity. However, the lack of comprehensive geophysical studies limits a more detailed investigation of their current state.

Mutnovsky Volcano is an active stratovolcano with a maximum elevation of 2,323 m, located approximately 15 km east of Gorely Volcano. According to the geological studies summarized by Selyangin (1993, 2009) and Simon et al. (2014), the volcano consists of four distinct stratocones that have developed since the Late Pleistocene. The oldest cones, Mutnovsky-I and -II, are located 3 km apart and were active 60–80 ka and 30–40 ka, respectively. These cones produced large volumes of lava and pyroclasts, totaling 58 and 24 km^3, respectively, with compositions ranging from basalts to rhyodacites. The Mutnovsky-III cone, located between cones I and II, has a significantly smaller volume of 5 km^3.

Mutnovsky Volcano features a large crater, measuring 1.5 × 2.0 km, formed by a violent explosive eruption. Several basaltic-andesitic cones and an extrusive dacitic dome, formed 4,000 years ago, are present inside the crater. The most recent cone, Mutnovsky-IV, hosting an active vent, originated around 11,000 years ago, approximately 1 km north from the center of the Mutnovsky-III crater. Mutnovsky-IV is composed of basaltic lavas and pyroclastic deposits, with a total volume of 3.8 km^3. Currently, it has a well-defined circular crater and exhibits strong, continuous degassing.

During the Holocene, Mutnovsky's activity has been primarily characterized by moderate phreatic and phreatomagmatic eruptions within its summit crater (Melekestsev et al., 1987). The most recent explosive eruption occurred in 1960 (Waltham, 2001). The volcano contains several fumarolic fields that emit significant volumes of gas. After a 40-year dormancy, hydrothermal explosions and ash emissions were recorded in the crater in March 2000 April 2007, May 2012 July 2013, February 2018, and spring 2020 (Kiryukhin et al., 2022). Geochemical analyses of radiogenic isotopes and trace elements in Mutnovsky's magmatic rocks indicate contamination of the mantle source with melt components from Gorely Volcano, suggesting trenchward mantle wedge corner flow (Duggen et al., 2007).

The Mutnovsky Geothermal Field, located in an elongated zone to the north of Mutnovsky Volcano, exhibits significant hydrothermal activity (see Figure 1c for details). The geological, hydrogeological, and thermal characteristics of the Mutnovsky geothermal area are described in studies by Vakin et al. (1986) and

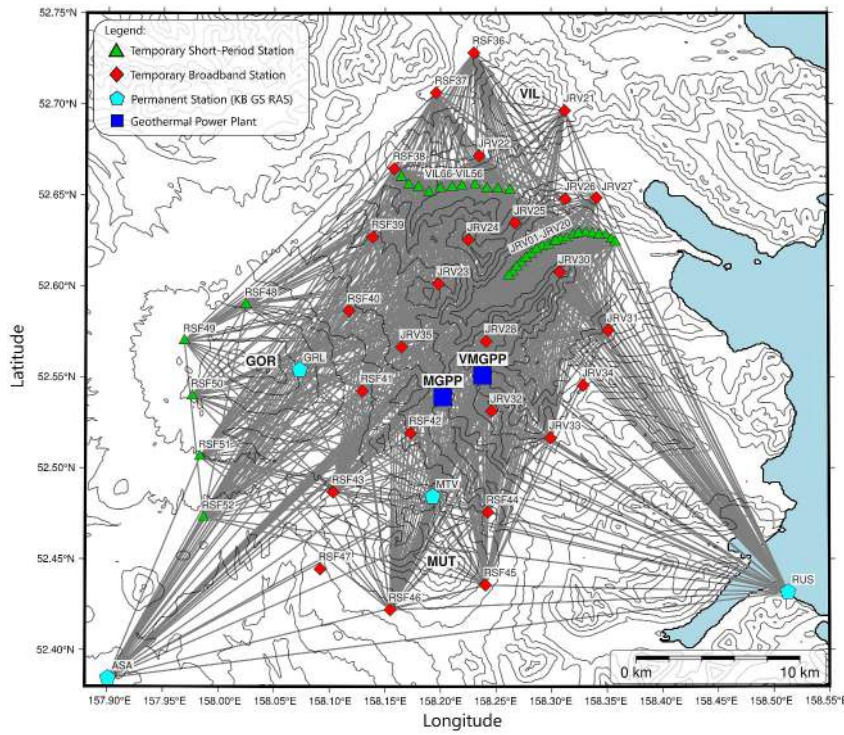

Figure 2. Distributions of seismic stations used in this study. The contours indicate the topography with the step of 200 m. The gray lines connect the station pairs with existing correlation functions used for ambient noise tomography. Abbreviations for volcanoes: GOR, Gorely; MUT, Mutnovsky; VIL, Viluchinsky. MGPP and VMGPP are the Mutnovsky and Verkhne-Mutnovsky Power Plants.

Sugrobov (1986). Strong degassing occurs at three distinct locations in the summit area of Mutnovsky Volcano: the Active Crater (1), Donnoe (2), and Upper (3) fumarolic fields. On the northern slope, two areas of hydrothermal activity are associated with the North-Mutnovsky fields (4 and 5). Existing boreholes, such as O35, produce significant steam output. The strongest hydrothermal activity is observed within the Dachny field (7) and its neighboring fields, Radon (8) and Medvezhy (9), where the Mutnovsky Geothermal Power Plant (GeoPP) is located. To the southeast of Dachny, the New field (6) became particularly active after 2003. In March 2024, a large ground collapse around borehole O22 resulted in the formation of a crater measuring 200 × 120 m laterally and reaching a depth of 30 m (Kiryukhin et al., 2025). Further north, several distinct thermal fields are observed in the Zhirovskoy and Vilyuchinsky Valleys, although the temperatures of these sources have declined in recent decades, likely due to the active exploitation of the Mutnovsky Geothermal Field.

3. Data Analysis

3.1. Seismic Records

In collaboration between industrial exploration (JSC "Zarubezhneft") and fundamental research (Russian Science Foundation, RSF) within Institute of Petroleum Geology and Geophysics Siberian Branch of the Russian Academy of Sciences (IPGG SB RAS), we deployed an extensive temporary seismic network around Mutnovsky and Gorely volcanoes. The network consisted of both short-period (SP) and broadband (BB) stations, supplemented by four permanent KB GS stations (ASA, GRL, MTV, RUS). To investigate the thermal fields, we installed two high-density survey lines in Zhirovskoy (20 SP stations) and Vilyuchinsky (10 SP stations) valleys. This integrated network provided great coverage, with 65 operational stations during 2023–2024. Detailed station geographical distribution is shown in Figure 2.

The deployment included a wide range of seismic equipment:

- Nanometrics Trillium PH broadband velocimeters (120 s period) with Nanometrics Centaur data loggers;
- Güralp CMG-6T broadband velocimeters (30 s period) with DiGOS Omnirecs DATA-CUBE3 data loggers;

- R-sensors CME-4111 broadband velocimeters (60 s period) with DiGOS Omnirecs DATA-CUBE3 data loggers;
- R-sensors CME-6111ND broadband velocimeters (60 s period) with integrated data loggers;
- Geospace GS-One LF 5 Hz short-period (0.2 s period) velocimeters with SPB-SI SCOUT data loggers;
- OKB IFZ SM3 short-period velocimeters (~0.8 Hz corner frequency) of the KB GS RAS's telemetered seismic stations network (Chebrov et al., 2013).

All SP stations exhibited extended frequency capabilities suitable for ambient noise tomography. This approach was inspired by the use of Mark L-4C-3D sensors, which have a nominal 1-s corner frequency, but have been successfully used for periods up to 20 s (Jaxybulatov et al., 2014). Pre-deployment field tests also confirmed the reliable performance of the GS-One sensors down to at least 0.1 Hz (10-s periods). Additionally, the CM-3 sensors from the KB GS RAS permanent network demonstrated reliable performance up to 10-s periods, as shown in previous studies of Kamchatka's North Volcano Group (Gómez-García et al., 2018; Soubestre et al., 2018, 2019). These short-period systems are particularly advantageous for dense temporary deployments due to their low power consumption, high reliability in extreme environments, and cost-effectiveness. This configuration enabled effective recovery of ambient noise signals across the network up to at least 10-s periods, making the short-period stations highly applicable for crustal-scale passive seismic surveys.

The seismic network operated with different sampling rates: broadband (BB) stations recorded at 100 Hz, temporary short-period (SP) stations equipped with GS-One stations were sampled at 125 Hz, and permanent stations maintained a fixed 200 Hz sampling rate.

3.2. Ambient Noise Correlation

This study focuses on the extraction and analysis of Rayleigh waves using vertical-component seismic records with daily duration. The processing workflow begins by defining frequency bands for all filtering procedures based on station type: 0.033–4 Hz for broadband (BB) stations and 0.1–4 Hz for short-period (SP) stations. Following Bensen et al. (2007), we apply the standard processing sequence as follows:

- Bandpass filtering within station-specific frequency ranges;
- Removal of instrumental responses;
- Removal of mean and linear trends followed by secondary bandpass filtering;
- Downsampling to 25 Hz for computational efficiency;
- Cutting records into 1-hr windows with a 50% overlap;
- Frequency domain normalization of the time-windowed signals using spectral whitening with spectral windowing in the frequency range;
- Time-domain normalization of the time-windowed signals by smoothed absolute value of prewhitened traces;
- Computation of hourly cross-correlation functions followed by linear stacking to produce daily cross-correlations.

In the daily cross-correlation gathers, we observe strong waveform changes beginning at the early February 2024 (Figure S1 in Supporting Information S1). These changes are concentrated around zero correlation times, suggesting the potential presence of seismovolcanic tremor activity (Gomez-Garcia et al., 2018; Green et al., 2020). To test this hypothesis, we investigate the eigenvalue distribution of the network's covariance matrix by estimating the spectral width (Seydoux et al., 2016). The spectral width serves as a proxy for the number of independent seismic sources detected by the network. A high spectral width indicates noise from multiple sources, while a low spectral width suggests a localized, coherent seismic source.

To identify the seismovolcanic signals, we selected 25 stations that operated continuously from October 2023 to May 2024. Using the CovSeisNet package (Tong et al., 2024), we computed the spectral width of the network covariance matrix with a 20-min averaging window and 50% overlap. The spectral width matrices (Figure S2 in Supporting Information S1) reveal that significant tremor activity began in early February 2024, characterized by a frequency band of 1.5–5 Hz. To mitigate the tremor's influence, we applied a 1 Hz low-pass filter to the daily cross-correlation gathers (Figure S1 in Supporting Information S1).

To further enhance the signal-to-noise ratio (SNR), we applied the singular value decomposition (SVD)-based Wiener filtering (Moreau et al., 2017) on the daily cross-correlation gathers (Figure S1 in Supporting Information S1). This procedure involved truncating the singular spectrum and applying Wiener filters to the singular

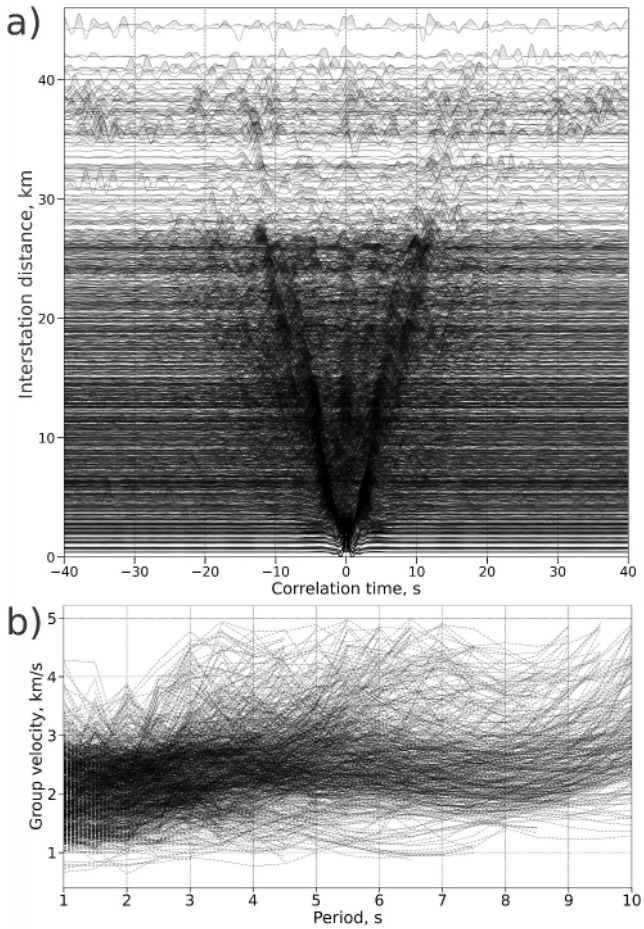

Figure 3. Data processing results: (a) all correlation functions ranged according to the interstation distances; (b) all dispersion curves before the quality control.

vectors, retaining only the top half of the singular values. We used a Wiener filter of 4 days and 1.1 s. Finally, we phase-weight stacked the daily cross-correlations (Green et al., 2020), applying a SNR selection criterion, where daily cross-correlations were excluded with SNR < 7.

Figure S3 in Supporting Information S1 shows the cross-correlation functions computed between different sensor types, revealing no significant visual differences between the results from broadband (BB) and short-period (SP) seismometers. This reaffirms the suitability of SP GS-One stations for seismic interferometry applications. Figure 3a presents the cross-correlation functions for all station pairs, organized by inter-station distance. These results consistently show well-defined Rayleigh waves dominating the empirical Green's functions. The station pairs producing the highest-quality surface wave signals are mapped in Figure 2, illustrating the spatial distribution of paths between station pairs.

We performed frequency-time analysis (FTAN) (Levshin et al., 1972) on all station-pair cross-correlation functions to extract Rayleigh wave group velocity dispersion curves. For each station pair, the FTAN was performed on the causal, acausal, and symmetrically averaged parts of the correlation function. The measurement from the variant yielding the highest signal-to-noise ratio and the most coherent dispersion curve was selected for subsequent tomographic inversion. This analysis provided over 1,000 high-quality dispersion measurements, which are shown in Figure 3b. The derived group velocities range from 1.0 to 5.0 km/s, reflecting substantial velocity heterogeneity within the medium, both laterally and vertically. However, some of these anomalous picks might be erroneous. Therefore, the following inversion procedure presumes a quality control with elimination of exessively large residuals.

4. Algorithms for 1D, 2D, and 3D Inversions of Surface Wave Data

In this study, we use the surface-wave tomography algorithm previously developed by Koulakov, Maksotova, et al. (2016). The process of optimizing a one-dimensional shear wave velocity model based on a given dispersion curve is illustrated in Figure S4 of Supporting Information S1. The 1D velocity distribution Vs(z) was determined to provide the best match between the calculated and observed average group velocity curves. The velocity model was adjusted iteratively based on the solution of the system of linear equations. For this purpose, sensitivity kernels were calculated, meaning the variations in the calculated group or phase velocity of the surface wave at a specific frequency (period) due to a unit variation in Vs(z) at a specific depth. The group velocity calculation for a given 1D Vp(z), Vs(z) and ρ(z) distributions was performed using a solver developed by Herrmann (2013). The calculated sensitivity kernels for the Rayleigh wave group velocity at periods from 0.5 to 10 s are shown in the lower left part of Figure S4 in Supporting Information S1. It can be seen, for example, that for a wave with a period of 0.5 s, the maximum sensitivity is achieved at zero depth; for 2 s, at a depth of 1 km; for 3.5 s, at a depth of 2 km; and for 6 s, at a depth of 6 km. It should be noted that as the periods increase, the absolute values of sensitivity decrease, meaning the stability of the solution becomes lower. Based on these sensitivity kernels, a system of linear equations is constructed, where the data vector is composed of residuals between the observed and calculated group velocities, and the unknown variables are the S-wave velocity deviations at different depths. This system is solved using the LSQR algorithm (Paige & Saunders, 1982). After inversion, the velocity model is updated, new sensitivity kernels are calculated, and a new inversion is performed. In our case, three iterations were performed to determine the average reference velocity model Vs(z). The resulting one-dimensional model is shown in the lower right part of Figure S4 in Supporting Information S1 (green line). The corresponding dispersion curve is presented in the upper part of the figure (green line). It can be seen that the observed average dispersion curve (red line) has a maximum in the period range of 4–5 s and a local minimum at 6–7 s. These variations correspond to a zone of

increased velocities at a depth of 4 km and a zone of reduced velocities around a depth of 6 km. Further, at greater depths, the velocity increases to 4.5 km/s.

Further steps in constructing a three-dimensional seismic model are based on the surface-wave tomography algorithm developed by Koulakov, Maksotova, et al. (2016). This algorithm involves calculations in two stages. At the first stage, two-dimensional maps of Rayleigh wave group velocities at various frequencies are calculated. For this purpose, all station pairs with available group velocity data at each frequency are selected, and ray paths are constructed using the bending method based on the Fermat's principle. During the first iteration, a constant velocity is used, but some deviations of waves due to topography are taken into account, because the surface waves follow the earth surface. In cases of strong topography features, the path with minimum time may be non-straight in the map view. The model is parameterized with nodes distributed in areas with sufficient ray coverage with a regular spacing (1.5 × 1.5 km in our case). A system of linear equations is supplemented with two additional blocks of equations controlling the amplitude and smoothness of the model. The coefficients for smoothing and amplitude damping (0.4 and 7, respectively), as well as the number of iterations (5) were determined according to the results of synthetic modeling to enable maximum resemblance of the original and recovered models. Note that changing these coefficients only affected the amplitudes of the anomalies, whereas the shapes of the anomalies remained stable for a large range of the varied parameters. The inversion is performed using the LSQR algorithm (Paige & Saunders, 1982) After performing the inversion, a two-dimensional velocity distribution is obtained, and new rays are constructed in the updated 2D distributions of group velocities using the bending method. In our case, we used five iterations. For data selection (Figure S6 in Supporting Information S1), in the first iteration, we excluded the data with time residuals exceeding 35% of the total travel time. In the following iterations, this threshold was reduced to 20% to filter outliers and improve model robustness. Examples of two-dimensional distributions of group velocity anomalies after five iterations for various periods are shown in Figure S7 of Supporting Information S1.

We calculated the values of the mean absolute time residuals (in L1 norm) and variance reduction for each period, which are presented in Table S1 of Supporting Information S1. It can be seen that at short periods, the values of variance reduction are larger than in cases of long periods indicating higher confidence of picking results in the high-frequency part. The distributions of the residuals computed in the starting flat and final 2D models of group velocities are shown in Figure S5 and S6 of Supporting Information S1. It can be seen that the inversion leads to more concentrated distributions of the residuals around a zero level. Note that the threshold to select the data was dependent on the absolute travel times. Therefore, for the long rays, large residualts were allowed, which are visible in the final plot on Figure S5 in Supporting Information S1.

Using the calculated group velocity distributions, local dispersion curves U(x,y,T) are obtained at each point in the study area. Using the one-dimensional forward modeling algorithm based on the solver by Herrmann (2013), a sensitivity matrix similar to the one shown in the lower left part of Figure S4 in Supporting Information S1 is calculated at each point (x,y) in the study area. After this, a simultaneous inversion is performed for the entire study volume, with additional constraints imposed on smoothing the velocity distribution and damping the amplitude of anomalies. Once the three-dimensional velocity model is obtained, new sensitivity kernels are calculated at each point (x,y), and the new inversion is performed. In our case, two iterations were carried out to obtain the final three-dimensional model Vs(x,y,z). Table S2 in Supporting Information S1 presents the root-mean-square of group velocity residuals and their reduction during the inversion procedure after two iterations. It can be seen that mean deviations of the observed and calculated group velocities in local dispesion curves varies from 0.0991 km/s in the 1D Vs model to 0.0325 km/s in the final 3D Vs model, which gives the variance reduction of 67.2%.

The resulting distributions of S-wave velocity anomalies are presented in horizontal sections (Figure 4) and in vertical profiles (Figure 5). The absolute values of the shear wave velocities are shown in the vertical cross-sections in Figure S8 of Supporting Information S1. Note that the horizontal sections display depths relative to the Earth's surface (e.g., the section at 0.2 km depth in Figure 4, for a plateau with an average elevation of ∼1,000 m, corresponds to ∼0.8 km above sea level). For the vertical sections, near-surface structures are plotted relative to the topography. At greater depths, the influence of topography is gradually phased out, becoming negligible below a predefined depth of 3 km. This approach reflects the physical reality that higher-frequency Rayleigh waves, which constrain shallow structures, are sensitive to topographic variations, whereas lower-frequency waves, which constrain deeper structures, are largely unaffected by topography.

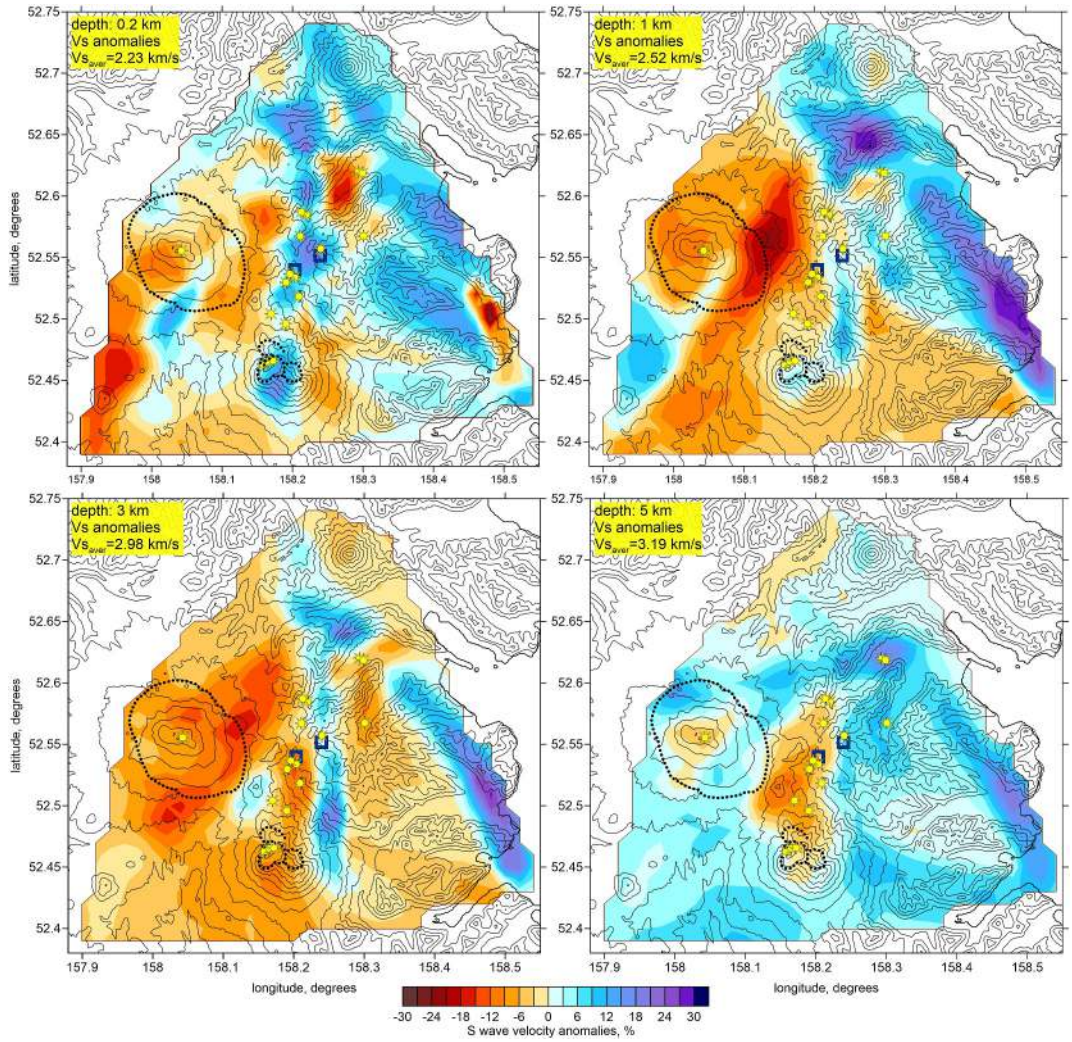

Figure 4. Horizontal sections of the three-dimensional distributions of shear wave velocity at different depths. The average velocities (Vsaver) are indicated in each panel. The yellow symbols are locations of hydrothermal discharges (fumaroles and hot springs), the dotted lines highlight the caldera of Gorely Volcano and the volcanic centers of Mutnovsky Volcano edifice and contour lines indicate topography with the interval of 200 m.

5. Synthetic Modeling

To assess the resolution of the obtained model, we performed synthetic tests. We employed several anomaly patterns, including a checkerboard model with alternating positive and negative anomalies, as well as free-shaped anomalies defined in horizontal and vertical sections. In all cases, the anomalies, expressed as percentage deviations, were superimposed onto a 1D S-wave velocity model. The inversion of the 3D structure was then performed using a separate 1D reference model, which was determined during the inversion procedure based on the recovered average group velocities.

Based on the synthetic model, the group velocities of Rayleigh waves at specific periods were calculated at each point (x,y) of the study area using the one-dimensional forward solver by Herrmann (2013). Next, in the obtained two-dimensional group velocity models, we calculated travel times for all available station pairs using the two-dimensional bending ray tracing algorithm. These travel times served as the synthetic data set, which was used to reconstruct the synthetic model through the exact same steps and with the same free parameters as in the inversion of the experimental data. The anomalies obtained from the inversion were compared with the original synthetic structures, and based on this comparison, we made conclusions about the resolution of the model.

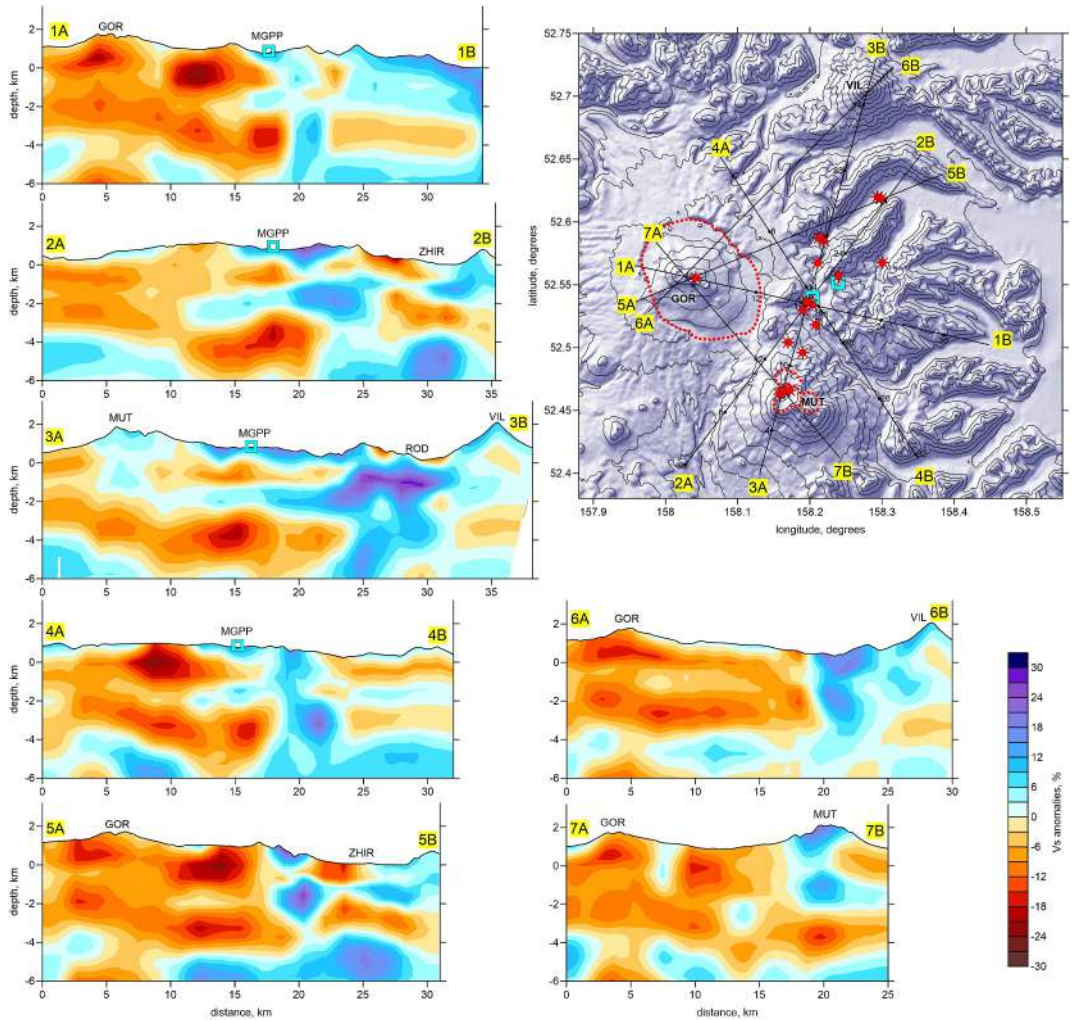

Figure 5. Vertical sections of the three-dimensional distributions of shear wave velocity anomalies. The locations of the sections are shown in the map. The red symbols in the map indicate the locations of hydrothermal discharges (fumaroles and hot springs), the red dotted lines highlight the caldera of Gorely Volcano and the volcanic centers of Mutnovsky Volcano edifice, and contour lines indicate topography with the interval of 200 m. Abbreviations for volcanoes: GOR, Gorely; MUT, Mutnovsky; VIL, Viluchinsky. MGPP is the Mutnovsky Geothermal Power Plant. ZHIR, Zhirovskaya Valley. ROD, Rodnikovaya.

In the first synthetic test, a checkerboard model was used as a synthetic velocity distribution, in which periodic rectangular anomalies with alternating signs were defined in all three dimensions. In Figure S9 in Supporting Information S1, these anomalies are shown by dashed lines in two horizontal and two vertical cross-sections. Figure S9 in Supporting Information S1 presents the recovery result of the three-dimensional checkerboard model with a horizontal anomaly size of 7 km and a vertical step of 4 km. It can be seen that, in general, the periodic structure of the anomalies is correctly reconstructed both horizontally and vertically. In horizontal sections at depths of 0.2 and 4.5 km, we can observe robust recovery of anomalies with opposite signs, corresponding to different layers in the model. However, in some parts of the area, significant smearing of the anomalies in the diagonal direction is observed, which is associated with the dominance of rays along the corresponding azimuths. This kind of smearing leads to some deformation of the anomalies, causing the boundaries of the reconstructed anomalies to shift relative to the true boundaries. There is also some deviation of the horizontal boundaries from their true positions, which is visible in the vertical cross-sections. Such artifacts must be taken into account when interpreting the results of the experimental data inversion.

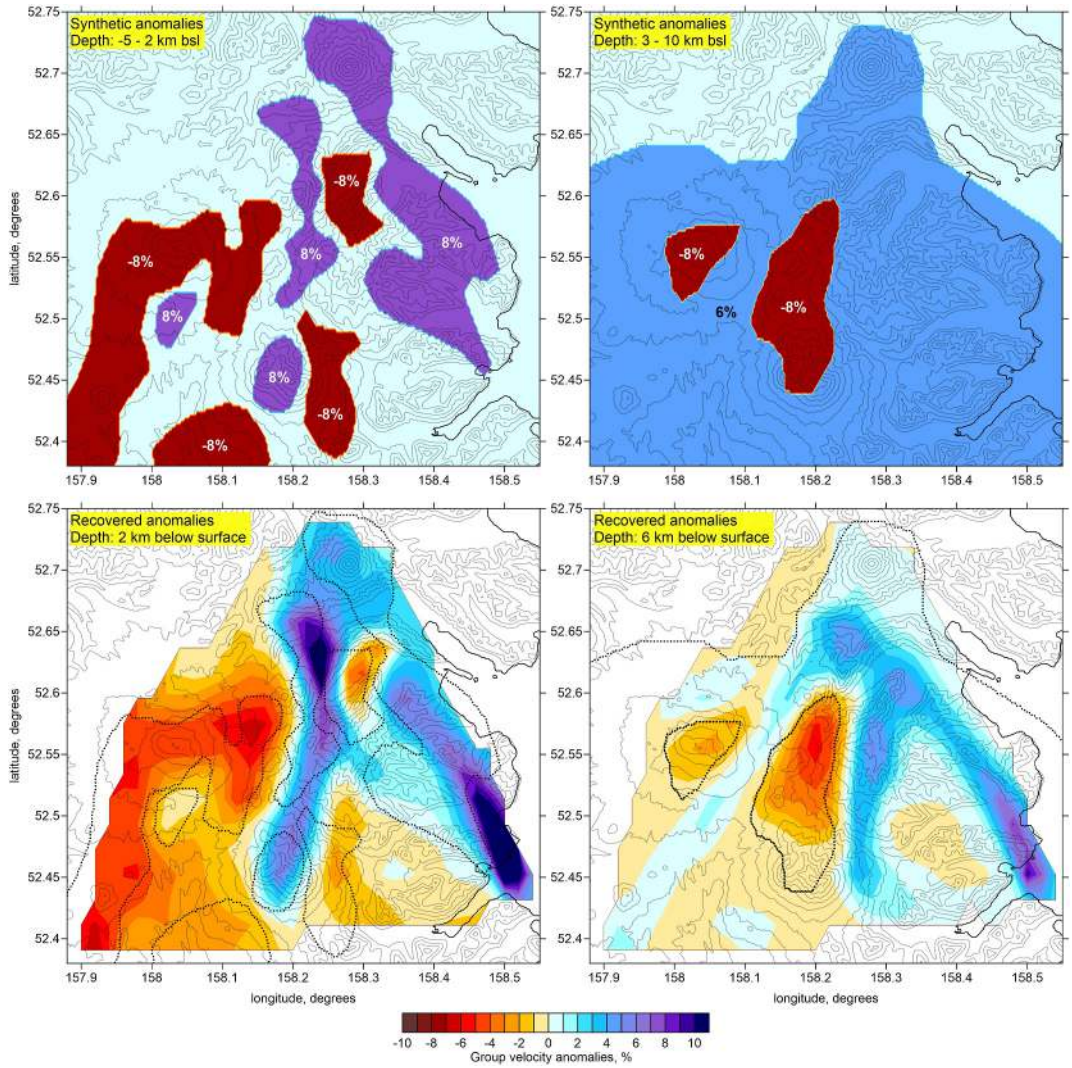

Figure 6. Synthetic test with realistic free-shaped anomalies defined in two depth intervals (upper row). The values of the original synthetic anomalies are indicated. Lower row presents the recovery results in two depth levels. The shapes of the original synthetic anomalies are depicted by dotted lines. Contour lines show the topography.

To evaluate the influence of rays from remote permanent stations on model artifacts, we performed an additional test excluding stations ASA and RUS (Figure S10 in Supporting Information S1). This test confirmed that the pronounced diagonal smearing artifacts in the peripheral regions are eliminated when these stations are removed. However, this also resulted in a loss of resolution in the central part of the model due to reduced ray coverage. Consequently, for the final model, we retained the full data set. The results in the marginal parts of the model, particularly features aligned with rays to these remote stations, should therefore be interpreted with caution.

In another test shown in Figure 6, synthetic anomalies with realistic shapes were defined by free-shaped polygonal blocks in two depth intervals. The amplitudes of the anomalies are indicated in maps with the original synthetic models (upper row in Figure 6). The recovery results show generally the same structures as defined in the model, which are similar to the results of the experimental data inversion. However, some details appear to be smeared due to the limited horizontal resolution. Also, at the depth of 6 km, we observe a phantom low-velocity anomaly in the southeastern part of the study area located in the area where a flat high-velocity anomaly was defined in the original model. The same structure is observed in the experimental data results (Figure 3), therefore it should be considered with prudence.

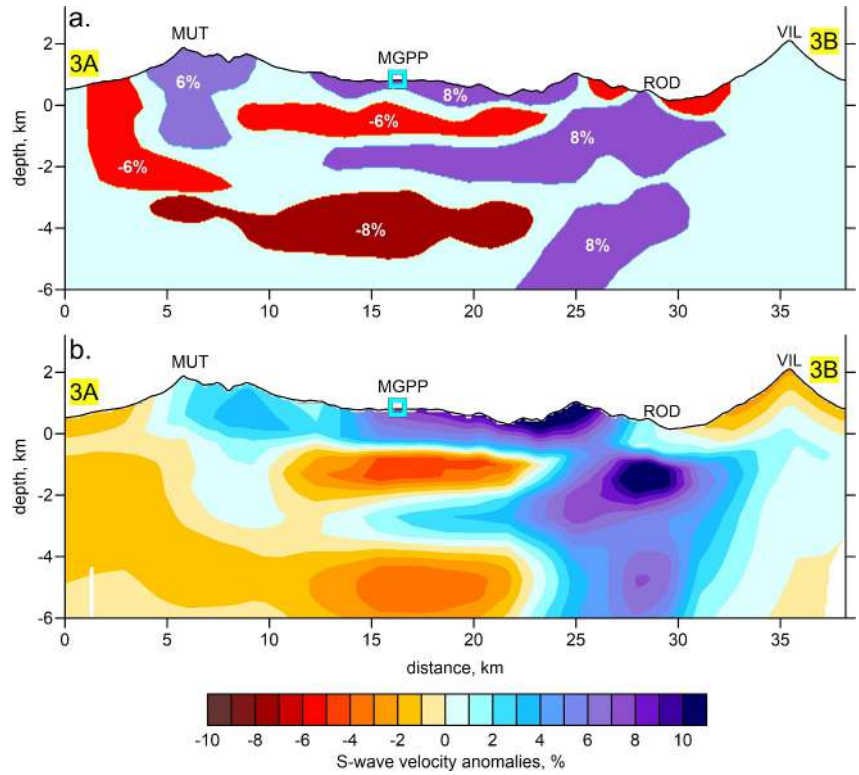

Figure 7. Synthetic test with free-shaped anomalies for vertical cross-section 3A-3B (see Figure 5 for location). (a) Original synthetic S-wave velocity model. Anomalies are defined as percentage deviations from the 1D reference model. (b) Model recovered through the full inversion procedure. The test demonstrates the algorithm's ability to resolve and distinguish between a deep magmatic storage and a shallower hydrothermal reservoir. Indications: MUT, Mutnovsky volcano; VIL, Vilyuchinsky volcano; MGPP, Mutnovsky Geothermal Power Plant; ROD, Rodnikovaya sources.

A final test was designed to evaluate the vertical resolution and separation of anomalies beneath the Mutnovsky Geothermal Plant. We constructed a synthetic model for a vertical cross-section (profile 3A-3B) in which the anomalies were set within polygonal prisms of free shape defined along the vertical section. In the perpendicular direction, the thickness of these prisms was defined as 10 km. Figure 7 presents a synthetic model containing a deep low-velocity body (representing a magmatic intrusion) and a separate, shallower low-velocity layer (representing a fluid-saturated reservoir). The inversion result demonstrates that the algorithm can robustly recover both anomalies and distinguish between them, supporting our interpretation of separate magmatic and hydrothermal sources beneath the MGPP. We note that the recovered anomalies in Figure 7 appear slightly deeper than their input counterparts. This minor depth shift is a known effect of the smoothing constraints applied during the inversion process. The regularization, which is necessary for stability in an ill-posed problem, tends to smear anomaly boundaries vertically, which can result in a downward bias for the recovered depth of shallow structures. Therefore, based on this test, we can infer that in the real model, the true positions of the near-surface anomalies are likely slightly shallower than they appear in the vertical sections.

6. Discussion of the Tomography Results

The results of the inversion of Rayleigh wave data from the regional seismic network are presented as shear wave velocity anomalies in four horizontal sections in (Figure 4) and seven vertical cross-sections in Figure 5. The absolute Vs velocities are shown in the vertical cross-sections in Figure S8 of Supporting Information S1.

In the horizontal cross-sections at depths of 0.2 and 1 km, the most prominent structure is a large low-velocity anomaly around Gorely Volcano, with an amplitude exceeding 20%. It can be assumed that this anomaly may be associated with the presence of a caldera around the volcano, which is filled with a thick layer of poorly consolidated sediments deposited after the catastrophic eruption occurred approximately 40,000 years ago (Braitseva et al., 1995; Selyangin, 2009). Since this caldera is a large depression in the topography, it accumulates

a significant amount of meteoric water, which can seep to great depths due to the high porosity of the rocks filling it. The poor consolidation of the sediments and the high water content are likely responsible for the anomalously low S-wave velocities to significant depths.

In vertical cross-sections 5 and 6 (Figure 5), we can see that the low-velocity anomaly beneath the Gorely volcano is distinctly stratified. At depths of up to 2 km, the most intense low-velocity anomaly is observed, which may be associated with the caldera deposits. Deeper, down to 4 km below the surface, another low-velocity anomaly is also observed, but it has a lower intensity and appears to be separated from the upper anomaly. This part may have a different origin, such as being related to the lateral intrusion of magmatic material into the crust. Interestingly, at depths from 4 to 6 km in vertical cross-sections 5, 6, and 7, directly beneath the summit of Gorely Volcano, a low-velocity column is observed, which may reflect the presence of a magma conduit. The same anomaly beneath the summit of the Gorely volcano is also clearly visible in the horizontal cross-section at a depth of 5 km (Figure 4).

Beneath the center of Mutnovsky Volcano, at shallow depths down to 1 km b.s.l., we observe a contrasting high-velocity anomaly, which may represent the rigid core of the stratovolcano. It should be noted that such high-velocity structures are observed beneath most stratovolcanoes for which seismic tomography studies have been conducted, such as Mt. Etna (Díaz-Moreno et al., 2018) and Vesuvius (Zollo et al., 1998), Teide on Tenerife (Koulakov, D'Auria et al., 2023) and Augustine in Alaska (Koulakov, Qaysi, et al., 2023). This kind of relationship is explained by the fact that large stratovolcanoes are formed through the accumulation of consolidated magmatic material, which has significantly higher velocities compared to the surrounding areas dominated by relatively loose and porous volcaniclastic sediments. Here, a fundamental difference between the Mutnovsky and Gorely volcanoes can be observed. While the core of the Mutnovsky stratovolcano was built over several hundred thousand years through the consolidation of intrusions composed of mostly basaltic magmatic material, the Gorely volcano experienced a powerful explosion ~40,000 years ago, which completely destroyed its old edifice and created a large depression—a caldera measuring 9 by 13 km. As a result, the Gorely volcano complex is dominated by low-velocity anomalies, whereas Mutnovsky volcano exhibits high-velocity anomalies.

As can be seen on cross-sections 3 and 7, directly beneath the crater of the Mutnovsky volcano, in the depth range from 2 to 5 km below sea level, an isometric low-velocity anomaly is observed, which may reflect the location of an active magma chamber beneath the volcano. This anomaly is also clearly visible in the horizontal cross-section at a depth of 5 km.

A prominent low-velocity anomaly is detected beneath the Mutnovsky Geothermal Power Plant (MGPP). In vertical cross-sections 1–4, the geometry of this anomaly can be traced in detail along multiple azimuths. The observations reveal an extensive low-velocity body at depths of 2–5 km, which likely represents an intrusive heat source retaining residual magma and/or partial melt. This deep anomaly may act as a magmatic reservoir, thermally driving meteoric fluid circulation in the upper crust. The presence of such a magma body beneath the Dachny springs is further supported by long-period seismic events, which were frequently recorded in 2024 near Dvugorbaya Sopka, adjacent to the MGPP. To investigate this seismicity, researchers from the KBGS deployed in the autumn of 2024 two additional seismic stations in close proximity to the geothermal plant.

It is instructive to compare the seismic tomography results with existing temperature estimates for the Mutnovsky geothermal field obtained by Kiryukhin et al. (2018) based on ~450 borehole measurements and hot spring temperature data. In Figure 8, we overlay contour lines of the temperature distribution at 250 m above sea level (corresponding to depths of 500–1,000 m below the surface) with velocity anomalies at 3 km depth below the surface. A striking correlation emerges: a pronounced low-velocity anomaly south of the MGPP coincides with a high-temperature zone (>220°C). This anomaly also encloses most hydrothermal activity manifestations. For instance, sources 6–9 (labeled in the figure) align with the peak amplitude of the low-velocity anomaly. Notably, the anomaly's center corresponds to the New-2003 geothermal field, where a major collapse in March 2024 formed a large crater (Kiryukhin et al., 2025).

The seismic tomography results at 3 km depth show the strongest correlation with the temperature distribution at 500–1,000 m below the surface. However, as seen in Figure 4, velocity anomalies at shallower depths exhibit an inverse relationship, with high-velocity anomalies coinciding with hydrothermal fields. These features suggest that the deep heat source at ~3 km depth and deeper (imaged as a low-Vs anomaly) controls the shallow thermal anomaly at 500–1,000 m depth. This overlay was chosen to visually demonstrate this causative link between the deep-seated magmatic intrusion and the shallower geothermal reservoir it heats. This suggests that the

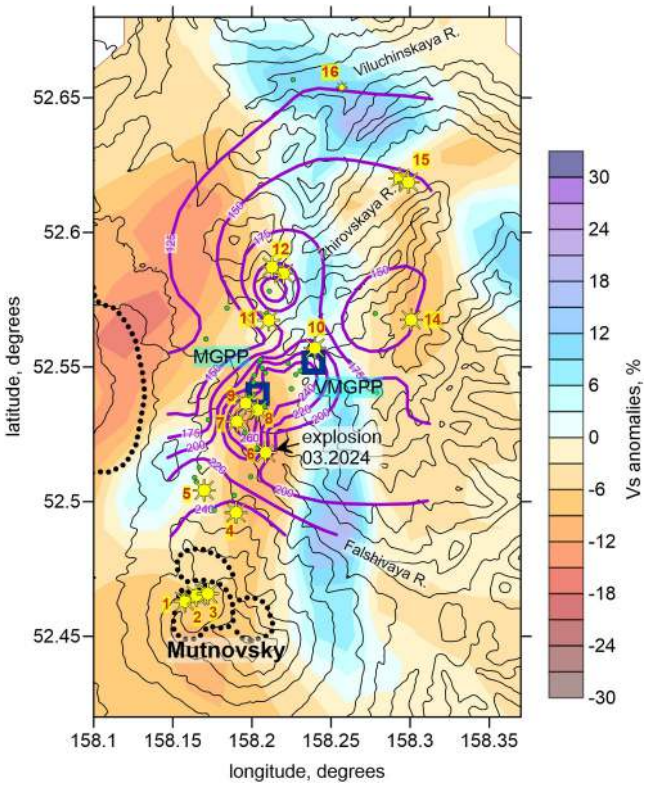

Figure 8. The resulting S-wave velocity distribution at the depth of 3 km b.s.l. Overlapped by the temperature distribution at a level of 0.25 km a.s.l. depicted by purple lines (Kiryukhin et al., 2018). The dotted lines highlight the caldera of Gorely Volcano and the volcanic centers of Mutnovsky Volcano edifice and contour lines indicate topography with the interval of 200 m. The yellow symbols are locations of hydrothermal discharges (fumaroles and hot springs): (1) Mutnovsky Active Crater; (2, 3) Donnoe and Upper fumarolic fields; (4, 5) North-Mutnovsky Fields; (6) New 2003; (7) Dachny; (8) Radon; (9) Medvezhy; (10) V-Mutnovsky; (11) Piratovsky hot springs; (12) V-Zhirovskoy; (14) Voinovsky Springs.

tomography model may delineate deep heat sources located beneath the productive formations that supply steam to the Mutnovsky Geothermal field.

The same structures are visible in Figure 9, which combines the seismic tomography inversion results in vertical section 3A-3B with complementary data from Kiryukhin et al. (2018) for the same profile, including the 3D temperature model cross-section, interpreted geological structures and projected boreholes with production intervals. The most striking feature in the tomography model is a low-velocity anomaly between 2.5 and 5 km depth (b.s.l.), centered directly beneath the MGPP. We interpret this as a hot magmatic body that heats the overlying hydrothermal reservoirs. While Kiryukhin et al. (2018; Figure 2) proposed a magma source in the same lateral position, their model placed it shallower (1–2 km b.s.l.). However, they acknowledged uncertainty about the source's exact depth, representing it schematically.

Figure 9 reveals that the magma-associated anomaly appears connected to a shallow low-velocity structure extending toward the surface along Mutnovsky Volcano's southern flank indicated by the downgoing blue arrows. We interpret this feature as a potential meteoric water aquifer, transporting surface-derived fluids to depths of ~3 km. This interpretation is supported by the fact that the S-wave velocities show particular sensitivity to liquid phases, with water-saturated layers typically exhibiting pronounced velocity reductions. While Kiryukhin et al. (2018) proposed a similar meteoric water circulation system, their model placed the recharge zone near the volcanic summit, whereas our model suggested the southern flank as the primary infiltration area.

Our interpretation scheme (Figure 9) suggests meteoric water may interact with the hot magmatic body, generating superheated fluids that ascend within an area corresponding to the distance of 10–12 km along the profile, as indicated by upgoing red arrows. A portion of these fluids may recirculate toward Mutnovsky Volcano's summit, potentially sustaining the observed fumarolic activity, though our tomography resolution remains insufficient to conclusively trace this pathway.

Most of the ascending fluids appear to accumulate beneath the Mutnovsky geothermal field, forming a shallow reservoir evidenced by a low-velocity layer near sea level (500–1,000 m depth below surface). This reservoir correlates spatially with both the production intervals of geothermal boreholes (marked by red stars in Figure 9) and the thermal anomaly's peak intensity at ~16 km along the profile, where Kiryukhin et al. (2018) temperature model shows the 100°C isotherm reaching its shallowest depth.

The hydrothermal-associated anomaly further extends northward from the MGPP location toward the Piratovsky and Verkhne-Zhirovskoy fields (labeled 11 and 12 in Figure 9). This deep structural connection may explain the fact of documented temperature decline in Verkhne-Zhirovskoy's hot springs following the Mutnovsky field's intensive exploitation since the early 2000s. Continuous low-velocity anomalies in our tomography model provide physical evidence supporting hydraulic connectivity between these spatially separated (>6 km) fields.

At the same time, our model reveals no connectivity between the Mutnovsky geothermal reservoir and the Vilyuchinsky Valley thermal springs (labeled 12 in Figure 9). The Zhirovskoy and Vilyuchinsky valleys are separated by a prominent high-velocity massif - likely remnants of the Zhirovskoy paleovolcano. This structural barrier consists of consolidated magmatic rocks, which typically exhibit high seismic velocities. Given this structural separation, the Vilyuchinsky hydrothermal variations likely represent an independent system unaffected by Mutnovsky's GPP operations. Instead, these thermal springs may derive their heat from alternative sources, potentially associated with the Gorely Volcano system where our tomography identifies another significant low-velocity anomaly.

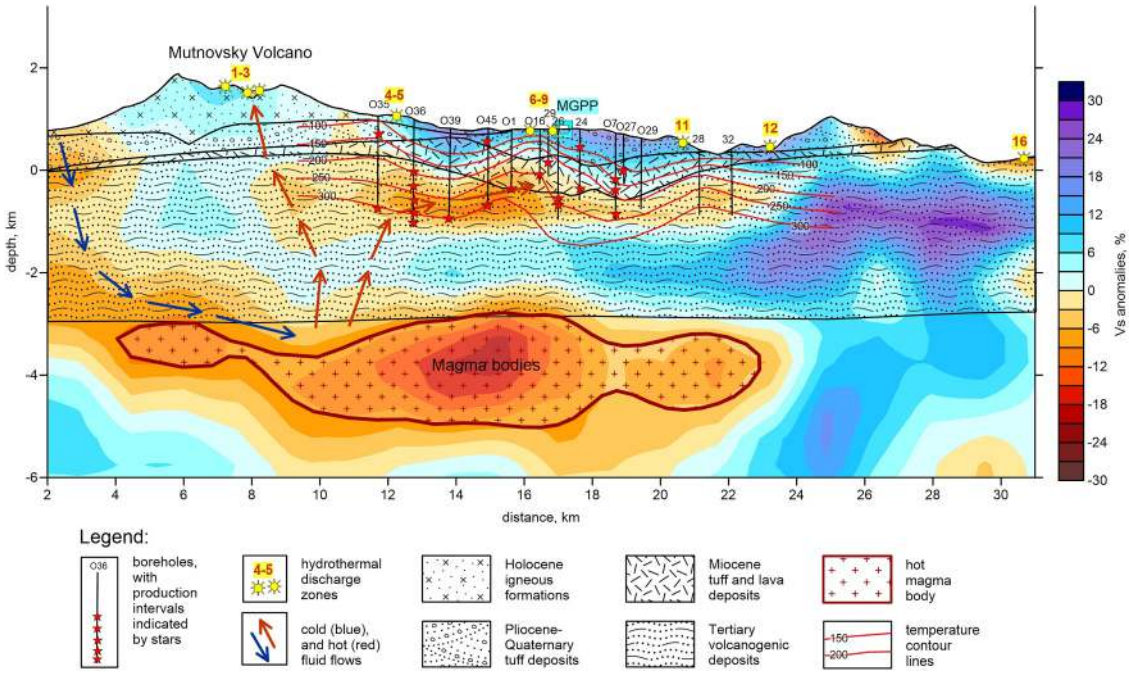

Figure 9. The distribution of the S-wave velocity in vertical Section 3 overlapped by a geological model and with projected boreholes from Kiryukhin et al. (2018). Stars indicate production intervals in the boreholes. Temperature distribution is estimated by Kiryukhin et al. (2018) based on measurements in the boreholes. The location of the magma body is retrieved based on the velocity model in this study. The yellow symbols are locations of hydrothermal discharges (fumaroles and hot springs): (1) Mutnovsky Active Crater; (2, 3) Donnoe and Upper fumarolic fields; (4, 5) North-Mutnovsky Fields; (6) New 2003; (7) Dachny; (8) Radon; (9) Medvezhy; (11) Piratovsky hot springs; (12) V-Zhirovskoy; (16) Vilychinsky Springs.

7. Conclusions

A dense joined seismic network of mixed broadband and short-period instruments was deployed across the Mutnovsky–Gorely–Vilyuchinsky volcanic complex (Kamchatka) during 2023–2024, with support from the Russian Science Foundation and JSC "Zarubezhneft." Ambient noise tomography applied to the data of this network produced the first crustal-scale three-dimensional S-wave velocity model based on over 1,000 Rayleigh wave dispersion curves. The model reveals distinct subsurface structures linked to regional volcanism and geothermal activity.

Beneath Gorely Volcano, a low-velocity anomaly coincides with its ∼40,000-year-old caldera deposits, suggesting deep infiltration of meteoric water. A secondary, less pronounced low-velocity anomaly at 2–4 km depth may reflect a lateral magmatic intrusion into the crust. In contrast, Mutnovsky Volcano features a central high-velocity core reflects its consolidated stratovolcanic edifice. Beneath this zone, an isometric low-velocity anomaly at 2–5 km depth below sea level likely corresponds to a Mutnovsky magma chamber.

A prominent low-velocity anomaly at 2.5–5 km depth beneath the Mutnovsky Geothermal Power Plant (MGPP) and Dachnye springs likely indicates a hot magmatic intrusion. This deep heat source connects to the surface via a fluid pathway along Mutnovsky's southern flank, where meteoric water reaches ∼3 km depths. Shallower anomalies (∼500–1,000 m depth) delineate the MGPP's production zone, matching both borehole data and existing temperature models. The strongest velocity reduction occurs 2–3 km south of MGPP, indicating potential untapped geothermal resources.

The model further demonstrates northward extension of these structures to the Zhirovskoy Valley's hydrothermal fields, supporting its connectivity with the Mutnovsky field and explaining observed temperature declines linked to MGPP operations. In contrast, no connectivity exists with Vilyuchinsky Valley's springs due to the intervening high-velocity Zhirovskoy paleovolcanic massif—a barrier of consolidated magmatic rocks. Vilyuchinsky's thermal regime appears independently fed, potentially by Gorely Volcano's magmatic system. These findings provide a robust framework for optimizing geothermal exploitation while assessing interconnected hydrological impacts across the volcanic complex.

Conflict of Interest

The authors declare no conflicts of interest relevant to this study.

Data Availability Statement

All the results of surface wave tomography, SURF_TOMO code and the dispersion curves presented in this study are accessible at Koulakov et al. (2025). All cross-correlation functions are available at Belovezhets et al. (2025). Figures 3, Figure S1–S3 in Supporting Information S1 were made with Matplotlib version 3.10.1 (Hunter, 2007; The Matplotlib Development Team, 2025), available under the Matplotlib license at https://matplotlib.org/. Figure 2 was created through PyGMT version 0.11.0 (Tian et al., 2024) using Generic Mapping Tools (GMT) version 6.5.0 (Wessel et al., 2019, 2024) licensed under LGPL version 3 or later, available at https://www.generic mapping-tools.org/. Figures 1, 4–9, Figure S4–S10 in Supporting Information S1 were made with Surfer® 13 from Golden Software, LLC (www.goldensoftware.com).

Acknowledgments

The temporal seismic networks installation was supported by JSC "Zarubezhneft" and Institute of Petroleum Geology and Geophysics SB RAS. The data from KB GS RAS permanent seismic stations was obtained with large-scale research facilities «Seismic infrasound array for monitoring Arctic cryolitozone and continuous seismic monitoring of the Russian Federation, neighbouring territories and the world» (https://ckp-rf.ru/usu/507436/) and provided within the state assignment according to the research project #075-00604-25 by DC. The data preparation was carried out by SA within the state assignment according to the research project FSUS-2025-0015. The contribution of IK, who performed the ambient noise tomography, was supported by the state assignment according to the research project FWZZ-2022-0017. We gratefully acknowledge Dr. Ruslan Zhostkov and Dr. Dmitry Presnov (Schmidt Institute of Physics of the Earth, RAS, Moscow) for providing 9 broadband integrated seismographs and participating in field operations. We also thank the administration of the Institute of the Earth's Crust SB RAS (Irkutsk) for supplying high-quality instruments for two additional broadband stations. Special appreciation is extended to Dr. Sergey Yaskevich, Dr. Alexandr Yablokov, Arkady Drobchik, Svyatoslav Ponasenko, and Nina Russkikh for their dedicated work in installing and dismantling this massive joint seismic network. We are especially grateful to the helicopter pilot Gennady Kroshkin for facilitating instrument deployment in remote areas, and to Ivan Boronin for expertly navigating Kamchatka's challenging terrain by truck.

References

Abramenkov, S., Shapiro, N. M., Koulakov, I., & Abkadyrov, I. (2020). Clustering of long-period earthquakes beneath Gorely volcano (Kamchatka) during a degassing episode in 2013. *Geosciences*, *10*(6), 230. https://doi.org/10.3390/geosciences10060230

Aiuppa, A., Giudice, G., Liuzzo, M., Tamburello, G., Allard, P., Calabrese, S., et al. (2012). First volatile inventory for Gorely volcano, Kamchatka. *Geophysical Research Letters*, *39*(6), 2012GL051177. https://doi.org/10.1029/2012GL051177

Avdeiko, G. P., Palueva, A. A., & Khleborodova, O. A. (2006). Geodynamic conditions of volcanism and magma formation in the Kurile-Kamchatka island-arc system. *Petrology*, *14*(3), 230–246. https://doi.org/10.1134/S0869591106030027

Belousov, V. I., Postnikov, A. I., Melnikov, D. V., & Belousova, S. P. (2005). *Geothermal Resourses*. Kamchatka Pedagogical State University.

Belovezhets, N., Berezhnev, Y., & Koulakov, I. (2025). Ambient noise cross-correlation functions computed for continious seismic data from temporary and permanent seismic stations operating in 2023–2024 around Mutnovsky and Gorely volcanoes (Kamchatka) [Dataset]. *Zenodo*. https://doi.org/10.5281/zenodo.17209099

Bensen, G. D., Ritzwoller, M. H., Barmin, M. P., Levshin, A. L., Lin, F., Moschetti, M. P., et al. (2007). Processing seismic ambient noise data to obtain reliable broad-band surface wave dispersion measurements. *Geophysical Journal International*, *169*(3), 1239–1260. https://doi.org/10.1111/j.1365-246X.2007.03374.x

Bijwaard, H., Spakman, W., & Engdahl, E. R. (1998). Closing the gap between regional and global travel time tomography. *Journal of Geophysical Research*, *103*(B12), 30055–30078. https://doi.org/10.1029/98JB02467

Bindeman, I. N., Leonov, V. L., Izbekov, P. E., Ponomareva, V. V., Watts, K. E., Shipley, N. K., et al. (2010). Large-volume silicic volcanism in Kamchatka: Ar–ar and U–Pb ages, isotopic, and geochemical characteristics of major pre-Holocene caldera-forming eruptions. *Journal of Volcanology and Geothermal Research*, *189*(1–2), 57–80. https://doi.org/10.1016/j.jvolgeores.2009.10.009

Braitseva, O. A., Melekestsev, I. V., Ponomareva, V. V., & Sulerzhitsky, L. D. (1995). Ages of calderas, large explosive craters and active volcanoes in the Kuril-Kamchatka region, Russia. *Bulletin of Volcanology*, *57*(6), 383–402. https://doi.org/10.1007/BF00300984

Bushenkova, N., Koulakov, I., Bergal-Kuvikas, O., Shapiro, N., Gordeev, E. I., Chebrov, D. V., et al. (2023). Connections between arc volcanoes in Central Kamchatka and the subducting slab inferred from local earthquake seismic tomography. *Journal of Volcanology and Geothermal Research*, *435*, 107768. https://doi.org/10.1016/j.jvolgeores.2023.107768

Chebrov, V. N., Droznin, D. V., Kugaenko, Y. A., Levina, V. I., Senyukov, S. L., Sergeev, V. A., et al. (2013). The system of detailed seismological observations in Kamchatka in 2011. *Journal of Volcanology and Seismology*, *7*(1), 16–36. https://doi.org/10.1134/S0742046313010028

Díaz-Moreno, A., Barberi, G., Cocina, O., Koulakov, I., Scarfì, L., Zuccarello, L., et al. (2018). New insights on Mt. Etna's crust and relationship with the regional tectonic framework from joint active and passive P-Wave seismic tomography. *Surveys in Geophysics*, *39*(1), 57–97. https://doi.org/10.1007/s10712-017-9425-3

Duggen, S., Portnyagin, M., Baker, J., Ulfbeck, D., Hoernle, K., Garbe-Schönberg, D., & Grassineau, N. (2007). Drastic shift in lava geochemistry in the volcanic-front to rear-arc region of the Southern Kamchatkan subduction zone: Evidence for the transition from slab surface dehydration to sediment melting. *Geochimica et Cosmochimica Acta*, *71*(2), 452–480. https://doi.org/10.1016/j.gca.2006.09.018

Egorushkin, I., Koulakov, I., Jakovlev, A., Huang, H.-H., Gordeev, E. I., Abkadyrov, I., & Chebrov, D. (2024). Crustal structure beneath Central Kamchatka inferred from ambient noise tomography. *Journal of Volcanology and Geothermal Research*, *449*, 108070. https://doi.org/10.1016/j.jvolgeores.2024.108070

Girina, O. A., Loupian, E. A., Sorokin, A. A., Melnikov, D. V., Romanova, I. M., Kashnitskii, A. V., et al. (2018). *Comprehensive monitoring of explosive volcanic eruptions of Kamchatka*. Institute of volcanology and seismology FEB RAS.

Gómez-García, C., Brenguier, F., Boué, P., Shapiro, N. M., Droznin, D. V., Droznina, S. Y., et al. (2018). Retrieving robust noise-based seismic velocity changes from sparse data sets: Synthetic tests and application to Klyuchevskoy volcanic group (Kamchatka). *Geophysical Journal International*, *214*(2), 1218–1236. https://doi.org/10.1093/gji/ggy190

Gontovaya, L. I., Popruzhenko, S. V., Nizkous, I. V., & Aprelkov, S. E. (2008). Upper mantle beneath Kamchatka: The depth model and its relation to tectonics. *Russian Journal of Pacific Geology*, *2*(2), 165–174. https://doi.org/10.1134/S1819714008020073

Gorbatov, A. (1999). Tomographic imaging of the P-wave velocity structure beneath the Kamchatka peninsula. *Geophysical Journal International*, *137*(2), 269. https://doi.org/10.1046/j.1365-246X.1999.00801.x

Gorbatov, A., Fukao, Y., Widiyantoro, S., & Gordeev, E. (2001). Seismic evidence for a mantle plume oceanwards of the Kamchatka-Aleutian trench junction. *Geophysical Journal International*, *146*(2), 282–288. https://doi.org/10.1046/j.0956-540x.2001.01439.x

Gorbatov, A., Kostoglodov, V., Suárez, G., & Gordeev, E. (1997). Seismicity and structure of the Kamchatka Subduction Zone. *Journal of Geophysical Research*, *102*(B8), 17883–17898. https://doi.org/10.1029/96JB03491

Gordeev, E. I., & Bergal-Kuvikas, O. V. (2022). Structure of the subduction Zone and volcanism in Kamchatka. *Doklady Earth Sciences*, *502*(1–2), 21–24. https://doi.org/10.1134/S1028334X22020088

Green, R. G., Sens-Schönfelder, C., Shapiro, N., Koulakov, I., Tilmann, F., Dreiling, J., et al. (2020). Magmatic and sedimentary structure beneath the Klyuchevskoy Volcanic Group, Kamchatka, from ambient noise tomography. *Journal of Geophysical Research: Solid Earth*, *125*(3), e2019JB018900. https://doi.org/10.1029/2019JB018900

Herrmann, R. B. (2013). Computer programs in seismology: An evolving tool for instruction and research. *Seismological Research Letters*, *84*(6), 1081–1088. https://doi.org/10.1785/0220110096

Hunter, J. D. (2007). Matplotlib: A 2D graphics environment. *Computing in Science and Engineering*, *9*(3), 90–95. https://doi.org/10.1109/mcse.2007.55

Jaxybulatov, K., Shapiro, N. M., Koulakov, I., Mordret, A., Landes, M., & Sens-Schonfelder, C. (2014). A large magmatic sill complex beneath the Toba caldera. *Science*, *346*(6209), 617–619. https://doi.org/10.1126/science.1258582

Jiang, G., Zhao, D., & Zhang, G. (2009). Seismic tomography of the Pacific slab edge under Kamchatka. *Tectonophysics*, *465*(1–4), 190–203. https://doi.org/10.1016/j.tecto.2008.11.019

Kiryukhin, A. V., Polyakov, A. Y., Sergeeva, A. V., Nuzhdaev, I. A., Zhuravlev, N. B., Voronin, P. O., et al. (2025). Magmatic activity of mutnovsky Volcano and crater formation at the site of blowing well 022. *Journal of Volcanology and Seismology*, *19*(4), 303–318. https://doi.org/10.1134/S0742046325700216

Kiryukhin, A. V., Polyakov, A. Y., Usacheva, O. O., & Kiryukhin, P. A. (2018). Thermal-permeability structure and recharge conditions of the Mutnovsky high-temperature geothermal field (Kamchatka, Russia). *Journal of Volcanology and Geothermal Research*, *356*, 36–55. https://doi.org/10.1016/j.jvolgeores.2018.02.010

Kiryukhin, A. V., Polyakov, A. Y., Voronin, P. O., Zhuravlev, N. B., Usacheva, O. O., Solomatin, A. V., & Kiryukhin, P. A. (2022). Magma fracking and production reservoirs beneath and adjacent to Mutnovsky volcano based on seismic data and hydrothermal activity. *Geothermics*, *105*, 102474. https://doi.org/10.1016/j.geothermics.2022.102474

Kiryukhin, A. V., & Sugrobov, V. M. (2019). Geothermal resources of Kamchatka and the nearest prospects of their development. *Journal of Volcanology and Seismology*, (6), 50–65. https://doi.org/10.31857/S0203-03062019650-65

Koulakov, I., Belovezhets, N., & Berezhnev, Y. (2025). Data and program codes to reproduce the results of surface-wave tomography for the area of Mutnovsky and Gorely volcanoes (Kamchatka) [Dataset]. *Zenodo*. https://doi.org/10.5281/ZENODO.15340118

Koulakov, I., D'Auria, L., Prudencio, J., Cabrera-Pérez, I., Barrancos, J., Padilla, G. D., et al. (2023). Local earthquake seismic tomography reveals the link between crustal structure and volcanism in tenerife (Canary Islands). *Journal of Geophysical Research: Solid Earth*, *128*(3), e2022JB025798. https://doi.org/10.1029/2022JB025798

Koulakov, I., Qaysi, S. I., Izbekov, P., & Browne, B. L. (2023). Structure of shallow magma sources beneath Augustine Volcano (Alaska) inferred from local earthquake tomography. *Journal of Volcanology and Geothermal Research*, *444*, 107965. https://doi.org/10.1016/j.jvolgeores.2023.107965

Koulakov, I. Y., Dobretsov, N. L., Bushenkova, N. A., & Yakovlev, A. V. (2011). Slab shape in subduction zones beneath the Kurile–Kamchatka and Aleutian arcs based on regional tomography results. *Russian Geology and Geophysics*, *52*(6), 650–667. https://doi.org/10.1016/j.rgg.2011.05.008

Koulakov, I. Y., Kukarina, E. V., Gordeev, E. I., Chebrov, V. N., & Vernikovsky, V. A. (2016). Magma sources in the mantle wedge beneath the volcanoes of the Klyuchevskoy group and Kizimen based on seismic tomography modeling. *Russian Geology and Geophysics*, *57*(1), 82–94. https://doi.org/10.1016/j.rgg.2016.01.006

Koulakov, I. Y., Maksotova, G., Jaxybulatov, K., Kasatkina, E., Shapiro, N. M., Luehr, B., et al. (2016). Structure of magma reservoirs beneath Merapi and surrounding volcanic centers of Central Java modeled from ambient noise tomography. *Geochemistry, Geophysics, Geosystems*, *17*(10), 4195–4211. https://doi.org/10.1002/2016GC006442

Kozhemyaka, N. N., Litasov, N. E., & Vazheevskaya, A. A. (1988). The Asacha group of volcanoes in Kamchatka. *Volcanology and Seismology*, *6*, 365–378.

Kugaenko, Y. A., & Nuzhdina, I. N. (2009). Low-frequency earthquakes of the Mutnovsky volcano. In *Problems of complex geophysical monitoring of the Russian far east. Second regional scientific and technical conference, Petropavlovsk-Kamchatsky, Russia (11-17 October 2009)*. Kamchatka Branch of Geophysical Service RAS.

Kugaenko, Y. A., Saltykov, V., Sinitsyn, V. I., & Chebrov, V. N. (2004). Emission tomography application to the localization of seismic noise sources associated with hydrothermal activity. *Izvestiya—Physics of the Solid Earth*, *40*, 149–162.

Kuznetsov, P., Koulakov, I., Jakovlev, A., Abkadyrov, I., Deev, E., Gordeev, E., et al. (2017). Structure of volatile conduits beneath Gorely volcano (Kamchatka) revealed by local earthquake tomography. *Geosciences*, *7*(4), 111. https://doi.org/10.3390/geosciences7040111

Lander, A. V., & Shapiro, M. N. (2007). The origin of the modern Kamchatka subduction zone. In J. Eichelberger, E. Gordeev, P. Izbekov, M. Kasahara, & J. Lees (Eds.), *Geophysical monograph series* (Vol. 172, pp. 57–64). American Geophysical Union. https://doi.org/10.1029/172GM05

Levina, V. I., Lander, A. V., Mityushkina, S. V., & Chebrova, A. Y. (2013). The seismicity of the Kamchatka region: 1962–2011. *Journal of Volcanology and Seismology*, *7*(1), 37–57. https://doi.org/10.1134/S0742046313010053

Levshin, A., Pisarenko, V. F., & Pogrebinsky, G. A. (1972). On a frequency-time analysis of oscillations. *Annals of Geophysics*, *28*, 211–218.

Melekestsev, I. V., Braitseva, O. A., & Ponomareva, V. V. (1987). Dynamics of Mutnovsky and Gorely volcanoes activity during the Holocene and volcanic hazard in adjacent areas (based on the data of tephrochronology). *Volcanology and Seismology*, *3*, 3–18.

Moreau, L., Stehly, L., Boué, P., Lu, Y., Larose, E., & Campillo, M. (2017). Improving ambient noise correlation functions with an SVD-based wiener filter. *Geophysical Journal International*, *211*(1), 418–426. https://doi.org/10.1093/gji/ggx306

Nurmukhamedov, A. G., Chernev, I. I., Alekseev, D. A., & Yakovlev, A. G. (2010). 3D geoelectric model of the Mutnov steam hydrothermal deposit. *Izvestiya—Physics of the Solid Earth*, *46*(9), 739–750. https://doi.org/10.1134/S106935131009003X

Pahkevich, R. I., Shadrin, A. V., & Chernev, I. I. (2018). Numerical thermohydrodynamic model of heat transfer in rocks of the Mutnovsky geothermal field prior to its industrial development. *Mining Informational and Analytical Bulletin*, *12*(60), 10–23. https://doi.org/10.25018/0236-1493-2018-12-60-10-23

Paige, C. C., & Saunders, M. A. (1982). LSQR: An algorithm for sparse linear equations and sparse least squares. *ACM Transactions on Mathematical Software*, *8*(1), 43–71. https://doi.org/10.1145/355984.355989

Ponomareva, V., Melekestsev, I., Braitseva, O., Churikova, T., Pevzner, M., & Sulerzhitsky, L. (2007). Late Pleistocene-Holocene volcanism on the Kamchatka peninsula, Northwest Pacific Region. In J. Eichelberger, E. Gordeev, P. Izbekov, M. Kasahara, & J. Lees (Eds.), *Geophysical monograph series* (Vol. 172, pp. 165–198). American Geophysical Union. https://doi.org/10.1029/172GM15

Romanova, I. M., Zelenin, E. A., Mikchaylyukova, P. G., & Ponomareva, V. V. (2015). Institute of Volcanology and Seismology FEB RAS geoportal and Kamchatka Holocene volcanism geoservice. *Geodesy and Cartography*, *902*(8), 17–23. https://doi.org/10.22389/0016-7126-2015-902-8-17-23

Seligman, A., Bindeman, I., Jicha, B., Ellis, B., Ponomareva, V., & Leonov, V. (2014). Multi-Cyclic and isotopically diverse silicic magma generation in an Arc Volcano: Gorely eruptive Center, Kamchatka, Russia. *Journal of Petrology*, *55*(8), 1561–1594. https://doi.org/10.1093/petrology/egu034

Selyangin, O. B. (1993). New data on Mutnovsky volcano: Structure, evolution and prediction. *Volcanology and Seismology*, *1*, 17–30.

Selyangin, O. B. (2009). *Wonderful world of Mutnovsky and Gorely volcanoes: Volcanologic and traveller's guide*. Hold. Komp."Novaya Kniga".

Senyukov, S. L. (2013). Monitoring and prediction of volcanic activity in Kamchatka from seismological data: 2000–2010. *Journal of Volcanology and Seismology*, *7*(1), 86–97. https://doi.org/10.1134/S0742046313010077

Seydoux, L., Shapiro, N. M., De Rosny, J., Brenguier, F., & Landès, M. (2016). Detecting seismic activity with a covariance matrix analysis of data recorded on seismic arrays. *Geophysical Journal International*, *204*(3), 1430–1442. https://doi.org/10.1093/gji/ggv531

Simon, A., Yogodzinski, G. M., Robertson, K., Smith, E., Selyangin, O., Kiryukhin, A., et al. (2014). Evolution and genesis of volcanic rocks from Mutnovsky Volcano, Kamchatka. *Journal of Volcanology and Geothermal Research*, *286*, 116–137. https://doi.org/10.1016/j.jvolgeores.2014.09.003

Sirin, A. N. (1958). The state of some volcanoes in Kamchatka at the beginning of 1957. *Bulletin of Volcanological Station*, 16–24.

Soubestre, J., Seydoux, L., Shapiro, N. M., De Rosny, J., Droznin, D. V., Droznina, S. Y., et al. (2019). Depth migration of seismovolcanic tremor sources below the Klyuchevskoy volcanic group (Kamchatka) determined from a network-based analysis. *Geophysical Research Letters*, *46*(14), 8018–8030. https://doi.org/10.1029/2019GL083465

Soubestre, J., Shapiro, N. M., Seydoux, L., de Rosny, J., Droznin, D. V., Droznina, S. Y., et al. (2018). Network-based detection and classification of seismovolcanic tremors: Example from the Klyuchevskoy volcanic group in Kamchatka. *Journal of Geophysical Research: Solid Earth*, *123*(1), 564–582. https://doi.org/10.1002/2017JB014726

Spichak, V., Schwartz, Y., & Nurmukhamedov, A. (2007). Conceptual model of the Mutnovsky geothermal deposit (Kamchatka) based on electromagnetic, gravity and magnetic data. *EGM 2007 International Workshop*. https://doi.org/10.3997/2214-4609-pdb.166.D_PP_02

Sugrobov, V. M. (1986). *Geochemical and geothermal methods of high-temperature thermal field investigation*. Nauka.

Syracuse, E. M., & Abers, G. A. (2006). Global compilation of variations in slab depth beneath arc volcanoes and implications. *Geochemistry, Geophysics, Geosystems*, *7*(5), 2005GC001045. https://doi.org/10.1029/2005GC001045

The Matplotlib Development Team. (2025). *Matplotlib: Visualization with python (version v3.10.1)*. Zenodo. https://doi.org/10.5281/ZENODO.14940554

Tian, D., Uieda, L., Leong, W. J., Schlitzer, W., Fröhlich, Y., Grund, M., et al. (2024). *PyGMT: A python interface for the generic mapping tools (version v0.11.0)*. Zenodo. https://doi.org/10.5281/ZENODO.10578540

Tokarev, P. I. (1984). Earthquake swarm of Asacha and its origin (Kamchatka, March–April, 1983). *Volcanology and Seismology*, *3*, 3–13.

Tong, F., Seydoux, L., & Journeau, C., & Soubestre, J. (2024). *covseisnet/covseisnet: Associate repository with a Zenodo DOI (1.0.0)*. Zenodo. https://doi.org/10.5281/ZENODO.10990032

Vakin, E. A., Pilipenko, G. F., & Sugrobov, V. M. (1986). General features of the Mutnovsky geothermal field and prognostic estimate of the resources. In *Geochemical and geothermal methods of high-temperature thermal field investigation* (pp. 6–41). Nauka.

Waltham, T. (2001). A guide to the volcanoes of southern Kamchatka, Russia. *Proceedings of the Geologists' Association, 112* (1), 67–78. https://doi.org/10.1016/S0016-7878(01)80051-1

Wessel, P., Luis, J. F., Uieda, L., Scharroo, R., Wobbe, F., Smith, W. H. F., & Tian, D. (2019). The Generic Mapping Tools Version 6. *Geochemistry, Geophysics, Geosystems*, *20*(11), 5556–5564. https://doi.org/10.1029/2019gc008515

Wessel, P., Luis, J. F., Uieda, L., Scharroo, R., Wobbe, F., Smith, W. H. F., et al. (2024). The Generic Mapping Tools version 6.5.0 (Version 6.5.0) [Computer software]. *Zenodo*. https://doi.org/10.5281/ZENODO.10119499

Zollo, A., Gasparini, P., Virieux, J., Biella, G., Boschi, E., Capuano, P., et al. (1998). An image of Mt. Vesuvius obtained by 2D seismic tomography. *Journal of Volcanology and Geothermal Research*, *82*(1–4), 161–173. https://doi.org/10.1016/S0377-0273(97)00063-2